HHS Public Access

Author manuscript

Mater Sci Eng C Mater Biol Appl. Author manuscript; available in PMC 2020 May 01.

Published in final edited form as:

Mater Sci Eng C Mater Biol Appl. 2019 May ; 98: 726–736. doi:10.1016/j.msec.2019.01.024.

The Effect of Surface Topography and Porosity on the Tensile Fatigue of 3D Printed Ti-6Al-4V Fabricated by Selective Laser Melting

Cambre N. Kelly[1], **Nathan T. Evans, Ph.D.**[2], **Cameron W. Irvin**[2,3], **Savita C. Chapman**[4], **Ken Gall, Ph.D.**[5], and **David L. Safranski, Ph.D.**[6]

[1]Department of Biomedical Engineering, Duke University

[2]School of Materials Science and Engineering, Georgia Institute of Technology

[3]Renewable Bioproducts Institute, Georgia Institute of Technology

[4]Department of Biomedical Engineering, Georgia Institute of Technology

[5]Department of Mechanical Engineering and Materials Science, Duke University

[6]MedShape, Inc.

Abstract

Additive manufacturing (3D printing) is emerging as a key manufacturing technique in medical devices. Selective laser melted (SLM) Ti-6Al-4V implants with interconnected porosity have become widespread in orthopedic applications where porous structures encourage bony ingrowth and the stiffness of the implant can be tuned to reduce stress shielding. The SLM technique allows high resolution control over design, including the ability to introduce porosity with spatial variations in pore size, shape, and connectivity. This study investigates the effect of construct design and surface treatment on tensile fatigue behavior of 3D printed Ti-6Al-4V. Samples were designed as solid, solid with an additional surface porous layer, or fully porous, while surface treatments included commercially available rotopolishing and SILC cleaning. All groups were evaluated for surface roughness and tested in tension to failure under monotonic and cyclic loading profiles. Surface treatments were shown to reduce surface roughness for all sample geometries. However, only fatigue behavior of solid samples was improved for treated as compared to non-treated surfaces Irrespective of surface treatment and resulting surface roughness, the fatigue strength of 3D printed samples containing bulk or surface porosity was approximately 10% of the ultimate tensile strength of identical 3D printed porous material. This study highlights the relative effect of surface treatment in solid and porous printed samples and the inherent decrease in fatigue properties of 3D printed porous samples designed for osseointegration.

Correspondence to: David L. Safranski.

Contact Information: Safranski: david.safranski@medshape.com.

Keywords

Selective laser melting; Ti-6Al-4V; fatigue; surface roughness; porosity

1. Introduction

Additive manufacturing of Ti-6Al-4V has become a leading method of producing medical devices with patient specific geometries and complex porous structures [1–6]. In orthopedics, numerous 3D-printed metallic implants have received FDA clearance for indications in spine, foot and ankle, and arthroplasty. Early successes of patient specific devices manufactured based on radiology data have shown that porous constructs can be successful in repairing critical-sized defects and achieving bone ingrowth [1, 7]. Powder bed fusion techniques, such as selective laser melting (SLM) and electron beam melting (EBM), are commonly used for the manufacture of Ti-6Al-4V implants. SLM utilizes a high-powered laser(s) to scan across a bed of material powder and selectively fuse particles to form the desired geometry layer by layer in which the printed geometry is defined by computer aided design (CAD). The use of SLM for manufacturing of Ti-6Al-4V scaffolds for orthopedic tissue engineering applications allows for control over complex geometries not possible with conventional manufacturing methods. The flexibility in design also allows for introduction of porosity, which has been introduced before using other manufacturing methods [8–10], but never with the same degree of control over total volume fraction, pore morphology, strut shape and size, and other intricate design inputs [11]. The introduction of porosity in scaffolds for tissue engineering applications creates a two-fold benefit: first reducing the effective modulus of the construct to within the range of native bone tissue, and second providing a three-dimensional structure for tissue ingrowth to reduce stress shielding and subsequent bone resorption [2, 7, 12]. While the fatigue strength of constructs decreases with increase in porosity [13], the introduction of interconnected repeating pores has already been shown to increase cellular response *in vitro* and *in vivo* [14–18]. Ideally, this increased osseointegration will lead to load sharing between implant and newly formed bone to facilitate the original load bearing function of the implantation site.

The material and mechanical properties of titanium alloy constructs are highly dependent on fabrication and post-processing conditions, including the microstructure which is dependent upon heat treatment parameters and cooling rate during processing [19–22]. In metal processing methods such as casting, the introduction of enclosed porosity and inclusions are sites for crack initiation, thus high temperature and pressure treatments are typical for improving fatigue strength. During the SLM process, the inherent speed of heating and cooling induces directionally dependent grain growth, internal porosity, and anisotropic microstructures [21]. Moreover, as each layer is cooled from its melt state, shrinkage occurs, inducing stress on the prior layer to which it is fused. Some steps can be taken to adapt printing parameters to decrease shrinkage [23], but typically additional post-processing heat treatments, such as stress relieving or hot isostatic pressing (HIP), are critical to reducing internal porosity, controlling the microstructure, and thus improving mechanical properties, particularly ductility [22]. As unwanted internal porosity is reduced, rough surface topography can play a significant role in fatigue strength as sites for fatigue crack

nucleation. Therefore, additional mechanical or chemical surface treatments are commonly used to reduce surface roughness in attempts to improve fatigue strength and biological response [14, 17, 18, 22, 24–31]. In orthopedic devices, which undergo repetitive loading, it is critical to examine not only the processing and postprocessing treatment parameters, but how these may dictate surface topography and the resulting mechanical properties for Ti-6Al-4V-based medical implants.

In addition, prior studies concerned with the fatigue performance of porous biomaterials, are often focused on compression fatigue resistance. Although in many load bearing applications, such as spinal and foot and ankle fusions, compression is the primary loading mechanism, it is also important to also evaluate fatigue loads in tension. Even when expected to be loaded only in compression, implants can sometimes experience tensile loads due to the stochastic nature of forces on the human body. In addition, scaffolds that are subject to far field compressive loading can have local tensile stresses through strut bending and other complex local stress states which may lead to complete failure at individual struts or nodes depending on the geometry of the pore [11, 32].

At present, the impact of surface roughness reduction on the tensile fatigue behavior of SLM samples with porous and solid structures is unknown. The objective of this work is to systematically determine the effect of both designed porosity and commercially available surface treatments on surface roughness and tensile fatigue behavior of SLM Ti-6Al-4V. Samples were designed as solid, solid with a surface porous layer, or fully porous. After printing, samples underwent a post-processing protocol which included: (1) standard HIP treatment, (2) a surface treatment, and (3) a standard anodization treatment. Characterization of the surface roughness, porous architecture, monotonic and fatigue tensile properties was conducted to determine the combined effect of porous design and surface treatment on the relationship between surface topography and fatigue performance.

2. Materials and Methods:

2.1 Additive Manufacturing and Post-Processing

Dogbone test specimens, as shown in Figure 1, were manufactured by selective laser melting of Ti-6Al-4V extra low interstitial (ELI) powder with a particle diameter range of 15–45 μm (3D Systems). Processing parameters were kept the same for all samples according to 3D Systems defined optimized scanning settings [33]. All test specimens were printed oriented in the z-direction (parallel to testing axis) on a titanium substrate in inert argon atmosphere (≤ 1.2 ppm O2). Three specimen designs were built: fully dense (solid) gage section, fully dense with an additional 0.5 mm porous layer on all sides of the gage section (surface porous), and a fully porous gage section (porous). For samples with porosity, the lattice structure was based on a repeating diamond unit cell geometry with a CAD designed pore size of 300–400μm. All samples underwent a three step post-processing protocol starting with HIP at 920°C at 1000 bar for 120 minutes [34]. Then samples underwent one of three possible surface treatments: no surface treatment, rotopolishing, or SILC cleaning. Following surface treatment, all samples were anodized to SAE AMS 2488D Type II [35]. Rotopolishing (3D Systems) is a proprietary multi-step mechanical polishing process involving multiple polishing media. Due to limitations in the process methods, rotopolishing

was not conducted for samples with any porosity and was only performed for solid samples. SILC cleaning (3D Systems) is a proprietary multi-step chemical cleaning process and was performed on all three sample designs. Solid wrought samples were waterjet cut from commercially available Ti-6Al-4V ELI sheet stock (3.2mm thick) parallel to the direction of rolling (hot-rolled, annealed 30 min at 1400°F, air cool, TIMET).

2.2 Surface Characterization:

Optical images were taken with a digital microscope (Keyence VHX-600) at 200× magnification. Surface roughness was measured using a laser confocal optical microscope at 20× with a wavelength cutoff of 100 μm (Olympus LEXT OLS4000 Confocal Microscope, n = 5/group). For porous and surface porous samples, roughness measurements were taking on exterior struts.

2.3 Micro-computed Tomography

Micro-computed tomography (Nikon XTH 225 ST) scans were taken for surface porous and fully porous samples to visualize and assess total porosity, strut spacing, and strut thickness. All scans were taken of the gauge section of each sample at 12 μm voxel size (150kV, 15.0 W, n=3/group). Images were reconstructed using CT Pro 3D software (Nikon). Volumetric reconstructions and evaluations were made with Avizo software (FEI) by preforming arithmetic operations on a thresholded sub-volume of the porous region to separate void space from material to calculate porosity. A space filling pore network model was used to assess strut spacing and thickness.

2.4 Mechanical Characterization:

Samples (n=3/group) were tested in tension to failure at a displacement rate of 1 mm/min on a 20-kip servo-controlled, hydraulically-actuated test frame (MTS Satec). Strain was captured using a high definition video camera (Canon HG10) and Image J software (NIH). For all stress calculations, the total area (defined by outer dimensions of gauge section of the dogbone) was used. Modulus was calculated using the tangent method from the initial linear region of the stress-strain curve. Fatigue tests were run at increasingly reduced stress levels below the yield strength of the samples to generate S-N curves and to determine the fatigue strength. Fatigue tests were run on the same test frame in axial stress control at a frequency of 5 Hz with R=0.1 ($n \geq 2$/stress level). Fatigue behavior is reported as both maximum applied stress and stress amplitude. Fatigue strength is defined as the stress amplitude at which samples reached 2,000,000 cycles without failure. Normalized fatigue strength (ratio of fatigue strength to ultimate tensile strength) is also reported. High cycle fatigue fracture surfaces were visualized with a scanning electron microscope (Hitachi S-3700N VP-SEM).

2.5 Statistical Analysis:

A one-way ANOVA with Tukey's post-hoc test was used to examine differences amongst solid samples with varying surface treatment. A two-way ANOVA with Tukey's post-hoc test was used to examine differences amongst samples with varying design and surface treatment. All data is expressed as average ± standard deviation, and all statistical analysis was computed using GraphPad Prism 7 software.

3. Results

Characterization of sample surfaces after the various surface treatments showed a range of topographies. Representative optical microscope images of the side of the gauge section of solid and surface porous dogbone surfaces are shown in Figure 2. The surface of rotopolish solid samples was visually smooth with slight surface marks present from the polishing process. The SILC clean solid samples showed some microtopographical roughness on the surface. The no-surface-treatment solid sample was covered with partially adhered powder particles that are typical of the laser melting process. No-surface-treatment surface porous samples showed similar coverage of partially adhered particles on the surface of struts. The SILC clean surface porous samples showed textured struts, but with less evidence of remnant partially adhered powder particles. The surface roughness of each sample is given in Table 1. For the solid samples, those with no surface treatment had a significantly greater roughness compared to all other solid samples ($p<0.01$). The SILC clean had a significantly greater roughness than the rotopolish samples ($p<0.05$). For the solid, surface porous, and porous samples that underwent no surface treatment or were SILC cleaned, the two-way ANOVA showed that the surface treatment (i.e. SILC or no-surface-treatment) was a statistically significant influence on local roughness ($p<0.01$), while design (i.e. porous versus flat) was not a statistically significant influence ($p=0.25$) on local roughness. Within each surface treatment, there were no significant differences in local roughness between porous and solid designs. When comparing between the surface treatments (i.e. no-surface-treatment vs SILC clean) the no-surface-treatment had a significantly greater roughness than the SILC clean ($p<0.01$) for each design (i.e. solid, surface porous, porous).

Figure 3 shows representative cross-sectional and volume rendering images of reconstructed microCT data of porous and surface porous samples. These cross-sections show the interconnected diamond lattice porosity in both the surface porous and porous structures. Table 2 provides a summary of analysis conducted on reconstructed volumes of surface porous and porous samples to determine porosity, average strut thickness, and average strut spacing. MicroCT analysis showed strut spacing at the lower end of the designed 300–400 μm range, and thus a reduction from the CAD defined porosity This deviation in as-built porosity from the 3D model is typical in AM parts and has been reported by others [36, 37], as defects, dross formation, and partially adhered powder on the surface of struts leads to over inflation of printed struts. No statistically significant difference was observed in porosity, average strut thickness, or average strut spacing amongst groups regardless of design or surface treatment.

Monotonic tensile testing was performed for all sample groups; exemplary stress-strain curves and summarized results are given in Figure 4 and Table 3 respectively. All SLM samples have similar overall mechanical behavior with a well-defined elastic region followed by yielding and plastic deformation; all samples failed within the gage section. Comparing the four solid samples (Figure 4A), there was no statistically significant difference in the elastic modulus. The three SLM solid samples had a significantly greater yield strength and ultimate tensile strength than the wrought sample ($p<0.01$). Also, the solid SILC clean had a significantly greater ultimate tensile strength than the solid no-surface-treatment ($p<0.05$). There was no statistically significant difference between the ultimate

tensile strength of the solid rotopolish samples compared to the no-surface-treatment or SILC clean samples. The failure strain of solid rotopolish and solid SILC clean samples was greater than the solid no-surface-treatment samples. Representative monotonic stress-strain curves of the SILC clean and no-surface-treatment porous and surface porous samples are shown in Figure 4B and Figure 4C respectively. For porous samples, there was no significant difference between no-surface-treatment and SILC clean samples for modulus, yield strength, ultimate tensile strength, or failure strain. For surface porous samples, ultimate tensile strength of SILC clean samples was significantly higher than no-surface-treatment samples ($p<0.01$). However, there was no significant difference in modulus, yield strength, or failure strain between surface porous SILC clean and no-surface-treatment samples.

Stress-life curves are given in Figure 5. The fatigue strength of solid samples increased as surface treatments were applied, where no-surface-treatment samples had the lowest fatigue strength, followed by SILC clean, and then rotopolish with the highest fatigue strength. The solid wrought samples (which underwent no surface treatment) had a fatigue strength the SILC clean 3D printed samples. The solid rotopolish fatigue curve displayed a sharper asymptotic behavior when approaching its fatigue strength, while the SILC clean and no-surface-treatment displayed a steadier decrease in strength as approaching respective failure or runout. Figure 5C and Figure 5D gives the stress-life curves of the porous and surface porous samples, represented as maximum stress and stress amplitude respectively. The fatigue strength of fully porous samples was independent of surface treatment with no difference between the surface treatment groups. SILC clean surface porous samples showed a small improvement in fatigue strength compared to the no-surface-treatment surface porous samples. A summary of results of fatigue properties for all groups is given in Table 4. Figure 6 shows normalized fatigue strength of all groups by roughness.

All fatigue sample failed within the gage section of the dogbone. Images of fracture surfaces of high cycle fatigue solid, surface porous, and fully porous samples are shown in Figure 7, 8, and 9 respectively. No internal porosity within the cross-section of the solid samples, the solid core of the surface porous, or the struts was observed. For all solid samples, cracks were seen to have initiated at the corners from the surface, leading to crack propagation followed by shear fracture. Surface porous samples also exhibited similar fracture behavior with crack initiation from a corner of the solid core which propagated across the cross section. Fully porous samples showed failure of a majority individual struts perpendicular to the loading axis, and some struts failing at a slant to the loading axis.

4. Discussion

This study examined the combined effects of porosity (as a surface layer or porous scaffold construct) and surface roughness (through post-processing surface treatments) on the tensile fatigue behavior of 3D printed Ti-6Al-4V samples. Samples were tested in tension to assess worst case scenarios for fatigue failure. The rectangular specimens used in this study were chosen because the corners, edges, and thickness provide a likeness to features found in orthopedic implants.

Orthopedic implants with highly interconnected porous surfaces and volumetric regions allow for bone ingrowth to create an interlock at the bone-implant interface, thus reducing issues with micromotion over time. Additionally, large porous regions reduce the effective modulus of implants, allowing load sharing with surrounding native bone to facilitate mechanotransduced bone remodeling over time. Table 5 provides porosity and pore morphology values for commercially available porous implants, including spinal implants and arthroplasty components, as well as porous constructs from published research. Typical porosity is greater than 60%, with spacing between struts (i.e. pores) ranging from 200–600μm. Samples in the present study had porosity lower than characteristic porous constructs, but strut thickness and spacing within the typical range. The reduction in the effective modulus of otherwise stiff metal constructs by incorporation of porosity is common in orthopedics but done at the cost of monotonic and fatigue strength. Implants should be designed to be robust to withstand mechanical failure, but with reduced stiffness and interconnected porosity for osseointegration applications. Surface porous samples in this study were representative of applications in which an additional porous layer is added to an existing implant's surface for ingrowth at the surface. Fully porous samples in this study were representative of applications in which substitution of solid material for a porous region would be done to reduce effective modulus, such as arthrodesis application. Thus the reported reduction in effective modulus to within the range of trabecular bone [38] is promising for designing implants to reduce stress shielding.

Achieving mechanical interlock of implant to bone also requires a surface topography and chemistry which is conducive to bone ingrowth. Without osteoblastic activity, fibrotic encapsulation of implants can occur, and contribute further to implant loosening and micromotion. Post-processing surface treatments and coatings have been studied to tailor chemical and physical properties of titanium surfaces to promote osteoblast activity and exclude fibroblasts [17, 18, 26, 31]. A recent study of SLM solid samples showed those which were grit blasted (Ra = 5.68 μm) resulted in a higher surface roughness compared to smooth titanium surfaces (Ra = 0.284 μm), and a subsequently higher bone to implant contact after 12 weeks in an in vivo ovine model [18], illustrating the tradeoffs seen between surface topography to balance mechanical and biological properties. Untreated SLM samples in this study were less rough than untreated surfaces produced by EBM [31], and close to some acid-etched and grit blasted samples [25, 26]. The wide variation of reported roughness values observed in the literature stems from highly varied treatment techniques. The chemical solution(s) and duration of exposure for chemical etching treatments are variable amongst comparable studies, thus it is not surprising that the SILC clean samples in this study were different from other reported acid etched surfaces [25, 26]. Even within the present study, the difference in surface treatments between rotopolishing (mechanical) and SILC cleaning (chemical) resulted in varied surfaces as expected. Additionally, surface treatment paradigms for samples produced via additive manufacturing, which require smoothing of the rough untreated surface, is converse to the innately smooth surfaces of traditionally manufactured surfaces which require roughening to induce biological response. It is expected that nano/microscale roughness of the no-surface-treatment and SILC clean surfaces would promote bone growth into pores. Alternatively, the rotopolished surface showed improved fatigue strength, but is likely lacking sufficient microtopography for

osseointegration applications. For solid constructs, SILC cleaning may provide a compromise by improving fatigue life compared to no-surface-treatment, while still maintaining a surface roughness conducive to osteoblast activity and bone formation. The optimization between surface roughness and fatigue strength depends on the clinical application and design to manage the cyclic loads experienced by the implant. A site with lower expected cyclic loading may be able to withstand a rougher surface as a tradeoff to encourage improved bone ingrowth.

Yield and ultimate tensile strength of all SLM solid samples were higher than that of the solid wrought samples, demonstrating that samples were sufficiently stress relieved and densified during the post-processing HIP cycle. As expected, porous samples had significantly lower yield strength, ultimate tensile strength, and failure strain than solid or surface porous samples. However, perhaps somewhat surprisingly, there was no significant difference in any monotonic mechanical properties between the no-surface-treatment and SILC clean porous samples. This result indicates that the effect of the fully porous structure dominates over that of surface roughness. Although porous structure wholly dominated monotonic properties in a full volumetric porous sample, the impact appears less dominant in the thin surface porous layer, in which ultimate tensile strength of surface porous samples did increase slightly after SILC cleaning.

No internal void porosity or defects were observed which have previously been shown as sites for early crack initiation [39], therefore fatigue performance was dependent on surface topography. As discussed above, surface roughness impacts the biological integration properties of implants, but can also be deleterious for fatigue strength. In general, rougher surfaces and porous structures lead to more stress concentration sites and reduced fatigue performance. In this study, the chosen commercially available surface treatments were used to compare the resulting surface and fatigue properties of both a physical (rotopolish) and chemical (SILC clean) treatment. The reduction in surface roughness following surface treatments reduced the sites for crack initiation from the surface of solid samples, thus improving the fatigue life. In solid rotopolished samples, the mechanical polishing process lead to rounding of the rectangular gage section of the dogbone geometry which likely contributed to the increase in fatigue life. Although the improvement in fatigue strength afforded by rotopolishing is desirable for orthopedic applications, the reduction in surface topography may prove detrimental to osseointegration. In agreement with the monotonic properties, the fatigue strength of fully porous samples was unaffected by SILC cleaning as compared to no-surface-treatment surfaces despite the significant reduction in local roughness. Similarly, for surface porous samples only a slight increase in fatigue strength is seen for SILC clean samples. Thus, the dominating effect of porous structure over surface roughness seen in monotonic properties is also observed in the fatigue strength of porous volumes. Analysis of the fracture surface for fully porous samples shows fracture of individual struts perpendicular to the loading axis, indicating cracks occurred at multiple individual struts until a critical decrease in load bearing area resulted in sample failure. Furthermore, for porous and surface porous samples, partially adhered particles are observable following SILC cleaning on interior struts. This indicates that the chemical SILC cleaning may not fully penetrate the pore network, thus resulting in crack initiation from interior struts as opposed to those at the corners.

Like wrought and cast Ti-6Al-4V, fatigue properties of SLM Ti-6Al-4V have been studied for a variety of processing conditions and geometries. While direct comparison of these varied processing methods is beneficial, it is non-trivial to compare varying sample geometries (thickness, notch factor), build orientation, heat/HIP treatments, surface treatments, and testing parameters. For example, the present study showed SILC clean solid samples had a maximum applied stress of 350 MPa at runout and 16% normalized fatigue strength. Similar maximum stress was reported for EBM [40] and SLM [41] samples by other groups, however a difference in testing parameters ($R= -1$) lead to a more than doubled normalized fatigue strength compared to the samples tested with $R=0.1$. Additionally, the fatigue strength of wrought specimens reported here is less than others previously reported, but this is attributed to the sharp corners and surface finish of the waterjet cut rectangular geometry [42]. Thus, summarized mechanical properties and roughness values along with testing parameters from the present and related literature are given in Table 6 and should always be considered when making comparisons of fatigue properties.

Figures 6A and 6B give visual representation of these normalized fatigue strengths versus roughness for current and referenced results. Implications of this comparison suggest that for solid samples, improvement to fatigue strength can be achieved with roughness reducing treatments; however, these treatments are negligible to improving fatigue strength of porous constructs. The results in the current study indicate that the local fatigue stress concentration due to the porous structures is high enough to reduce fatigue life irrespective of local surface roughness. Similar designs to the porous samples studied here have previously proven to provide a scaffold for cellular ingrowth and subsequent bone formation [17, 18, 31]. However, the cost of this increased biological response achieved through surface roughness and porous microarchitecture leads to a reduction in fatigue performance. The surface porous samples studied here provide a layer of porosity for ingrowth which may increase implant stability over time, and with increased (non-normalized) fatigue strength compared to fully porous samples. Cellular ingrowth requires high interconnectivity and pore size of approximately 200–500μm [43, 44], which is achievable with selective laser melting methods. In many studies, volumetric ingrowth or total area of new bone measured from an explanted scaffold sample is used when assessing relative performance between experimental groups [43, 45]. However, measurement of linear through-growth from the bone-implant interface is less well studied. The understanding of distance (depth) of ingrowth into porous constructs from a contact surface with native tissue would enable optimization of the tradeoff between porous and solid regions. Implant retrieval studies have shown significant difference in maximum depth of ingrowth between anatomical sites [46, 47]. These results motivate the need for design and fabrication of implants with sufficiently thick surface porosity to create a bone-implant interlock, and a solid core for fatigue resistance. Additionally, more recent research has investigated the fabrication of functionally graded lattice designs [48]. These graded porous scaffolds could be designed with larger pores at the surface to promote cellular ingrowth and transition to higher volume fraction at the core to tune stiffness of the construct [32, 49].

5. Conclusion

Additive manufacturing is becoming widely used in the development of medical devices, especially implants with complex surfaces, microarchitectural porosity, and patient-specific geometries. Selective laser melting of Ti-6Al-4V provides flexibility in the design of implants intended for bone fusion applications while sustaining superior mechanical properties for load bearing during bone ingrowth. Current designs in orthopedic devices seek bone ingrowth to surface porosity to establish interfacial bone-implant contact, or volumetric growth into a highly porous interconnected region of an implant. In this study, it was observed that rotopolishing and SILC cleaning treatments reduced surface roughness of SLM surfaces. Solid samples from the current study showed a trend of improving normalized fatigue strength with reduction in roughness. However, for samples with porous regions, a reduction in roughness after surface treatment caused no improvement in fatigue strength. The presented results and comparisons to related literature contextualize interesting design tradeoffs of implants for load-bearing applications.

Acknowledgements

This work was funded in part by NIH NIAMS SBIR 1R43AR068864. This work was performed in part at the Georgia Tech Institute for Electronics and Nanotechnology, a member of the National Nanotechnology Coordinated Infrastructure, which is supported by the National Science Foundation (Grant ECCS-1542174).

References

[1]. Hamid KS, Parekh SG, Adams SB, Salvage of Severe Foot and Ankle Trauma With a 3D Printed Scaffold, Foot Ankle Int, 37 (2016) 433–439. [PubMed: 26764314]

[2]. Mullen L, Stamp RC, Brooks WK, Jones E, Sutcliffe CJ, Selective Laser Melting: a regular unit cell approach for the manufacture of porous, titanium, bone in-growth constructs, suitable for orthopedic applications, J Biomed Mater Res B Appl Biomater, 89 (2009) 325–334. [PubMed: 18837456]

[3]. Telfer S, Pallari J, Munguia J, Dalgarno K, McGeough M, Woodburn J, Embracing additive manufacture: implications for foot and ankle orthosis design, BMC Musculoskelet Disord, 13 (2012) 84. [PubMed: 22642941]

[4]. Wong KC, Kumta SM, Geel NV, Demol J, One-step reconstruction with a 3D-printed, biomechanically evaluated custom implant after complex pelvic tumor resection, Comput Aided Surg, 20 (2015) 14–23. [PubMed: 26290317]

[5]. Smith KE, Dupont KM, Safranski DL, Blair JW, Buratti DR, Zeetser V, Callahan R, Lin JS, Gall K, Use of 3D printed bone plate in novel technique to surgically correct hallux valgus deformities, Techniques in Orthopaedics, 31 (2016) 181–189. [PubMed: 28337049]

[6]. Kelly CN, Miller AT, Hollister SJ, Guldberg RE, Gall K, Design and Structure–Function Characterization of 3D Printed Synthetic Porous Biomaterials for Tissue Engineering, Advanced healthcare materials, 7 (2018) 1701095.

[7]. Anne-Marie Pobloth SC, Razi Hajar, Petersen Ansgar, Weaver James C., Schmidt-Bleek Katharina, Windolf Markus, Tatai Andras Á., Roth Claudia P., Schaser Klaus-Dieter, Duda Georg N., Schwabe Philipp, Mechanobiologically optimized 3D titanium-mesh scaffolds enhance bone regeneration in critical segmental defects in sheep, DOI.

[8]. Wen CE, Yamada Y, Shimojima K, Chino Y, Hosokawa H, Mabuchi M, Novel titanium foam for bone tissue engineering, Journal of Materials Research, 17 (2011) 2633–2639.

[9]. Torres Y, Pavón JJ, Rodríguez JA, Processing and characterization of porous titanium for implants by using NaCl as space holder, Journal of Materials Processing Technology, 212 (2012) 1061–1069.

[10]. Niu W, Bai C, Qiu G, Wang Q, Processing and properties of porous titanium using space holder technique, Materials Science and Engineering: A, 506 (2009) 148–151.

[11]. Zadpoor AA, Mechanics of additively manufactured biomaterials, J Mech Behav Biomed Mater, 70 (2017) 1–6. [PubMed: 28433241]

[12]. Krishna BV, Bose S, Bandyopadhyay A, Low stiffness porous Ti structures for load-bearing implants, Acta Biomater, 3 (2007) 997–1006. [PubMed: 17532277]

[13]. Yavari SA, Wauthle R, van der Stok J, Riemslag AC, Janssen M, Mulier M, Kruth JP, Schrooten J, Weinans H, Zadpoor AA, Fatigue behavior of porous biomaterials manufactured using selective laser melting, Mater Sci Eng C Mater Biol Appl, 33 (2013) 4849–4858. [PubMed: 24094196]

[14]. Cheng A, Cohen DJ, Boyan BD, Schwartz Z, Laser-Sintered Constructs with Bio-inspired Porosity and Surface Micro/Nano-Roughness Enhance Mesenchymal Stem Cell Differentiation and Matrix Mineralization In Vitro, Calcif Tissue Int, 99 (2016) 625–637. [PubMed: 27501817]

[15]. Cohen DJ, Cheng A, Kahn A, Aviram M, Whitehead AJ, Hyzy SL, Clohessy RM, Boyan BD, Schwartz Z, Novel Osteogenic Ti-6Al-4V Device For Restoration Of Dental Function In Patients With Large Bone Deficiencies: Design, Development And Implementation, Sci Rep, 6 (2016) 20493. [PubMed: 26854193]

[16]. Pattanayak DK, Fukuda A, Matsushita T, Takemoto M, Fujibayashi S, Sasaki K, Nishida N, Nakamura T, Kokubo T, Bioactive Ti metal analogous to human cancellous bone: Fabrication by selective laser melting and chemical treatments, Acta Biomater, 7 (2011) 1398–1406. [PubMed: 20883832]

[17]. Cohen DJ, Cheng A, Sahingur K, Clohessy RM, Hopkins LB, Boyan BD, Schwartz Z, Performance of laser sintered Ti-6Al-4V implants with bone-inspired porosity and micro/nanoscale surface roughness in the rabbit femur, Biomed Mater, 12 (2017) 025021. [PubMed: 28452335]

[18]. Svehla M, Morberg P, Zicat B, Bruce W, Sonnabend D, Walsh WR, Morphometric and mechanical evaluation of titanium implant integration: comparison of five surface structures, J Biomed Mater Res, 51 (2000) 15–22. [PubMed: 10813740]

[19]. Pederson R, Microstructure and Phase Transformation of Ti-6Al-4V, Applied Physics and Mechanical Engineering, Lulea University of Technology, 2002.

[20]. Venkatesh BD, Chen DL, Bhole SD, Effect of heat treatment on mechanical properties of Ti–6Al–4V ELI alloy, Materials Science and Engineering: A, 506 (2009) 117–124.

[21]. Thijs L, Verhaeghe F, Craeghs T, Humbeeck JV, Kruth J-P, A study of the microstructural evolution during selective laser melting of Ti–6Al–4V, Acta Materialia, 58 (2010) 3303–3312.

[22]. Vrancken B, Thijs L, Kruth J-P, Van Humbeeck J, Heat treatment of Ti6Al4V produced by Selective Laser Melting: Microstructure and mechanical properties, Journal of Alloys and Compounds, 541 (2012) 177–185.

[23]. Liu Y, Yang Y, Wang D, Investigation into the shrinkage in Z-direction of components manufactured by selective laser melting (SLM), The International Journal of Advanced Manufacturing Technology, 90 (2016) 2913–2923.

[24]. Amin Yavari S, Wauthle R, Böttger AJ, Schrooten J, Weinans H, Zadpoor AA, Crystal structure and nanotopographical features on the surface of heat-treated and anodized porous titanium biomaterials produced using selective laser melting, Applied Surface Science, 290 (2014) 287–294.

[25]. Boyan BD, Batzer R, Kieswetter K, Liu Y, Cochran DL, Szmuckler-Moncler S, Dean DD, Schwartz Z, Titanium surface roughness alters responsiveness of MG63 osteoblast-like cells to 1 alpha,25-(OH)2D3, J Biomed Mater Res, 39 (1998) 77–85. [PubMed: 9429099]

[26]. D'Lima DD, Lemperle SM, Chen PC, Holmes RE, Colwell CW, Jr., Bone response to implant surface morphology, J Arthroplasty, 13 (1998) 928–934. [PubMed: 9880187]

[27]. Bagno A, Di Bello C, Surface treatments and roughness properties of Ti-based biomaterials, J Mater Sci Mater Med, 15 (2004) 935–949. [PubMed: 15448401]

[28]. Cheng A, Humayun A, Cohen DJ, Boyan BD, Schwartz Z, Additively manufactured 3D porous Ti-6Al-4V constructs mimic trabecular bone structure and regulate osteoblast proliferation,

differentiation and local factor production in a porosity and surface roughness dependent manner, Biofabrication, 6 (2014) 045007. [PubMed: 25287305]

[29]. Pyka G, Kerckhofs G, Papantoniou I, Speirs M, Schrooten J, Wevers M, Surface Roughness and Morphology Customization of Additive Manufactured Open Porous Ti6Al4V Structures, Materials (Basel), 6 (2013) 4737–4757. [PubMed: 28788357]

[30]. Hyzy SL, Olivares-Navarrete R, Schwartz Z, Boyan BD, BMP2 induces osteoblast apoptosis in a maturation state and noggin-dependent manner, J Cell Biochem, 113 (2012) 3236–3245. [PubMed: 22628200]

[31]. Bertollo N, Da Assuncao R, Hancock NJ, Lau A, Walsh WR, Influence of electron beam melting manufactured implants on ingrowth and shear strength in an ovine model, J Arthroplasty, 27 (2012) 1429–1436. [PubMed: 22503332]

[32]. Lietaert K, Cutolo A, Boey D, Van Hooreweder B, Fatigue life of additively manufactured Ti6Al4V scaffolds under tension-tension, tension-compression and compression-compression fatigue load, Sci Rep, 8 (2018) 4957. [PubMed: 29563593]

[33]. Wauthle R, Vrancken B, Beynaerts B, Jorissen K, Schrooten J, Kruth J-P, Van Humbeeck J, Effects of build orientation and heat treatment on the microstructure and mechanical properties of selective laser melted Ti6Al4V lattice structures, Additive Manufacturing, 5 (2015) 77–84.

[34]. Weißmann V, Drescher P, Bader R, Seitz H, Hansmann H, Laufer N, Comparison of Single Ti6Al4V Struts Made Using Selective Laser Melting and Electron Beam Melting Subject to Part Orientation, Metals, 7 (2017) 91.

[35]. Anodic Treatment - Titanium and Titanium Alloys Solution pH 13 or Higher, SAE International, 2018.

[36]. Liu YJ, Wang HL, Li SJ, Wang SG, Wang WJ, Hou WT, Hao YL, Yang R, Zhang LC, Compressive and fatigue behavior of beta-type titanium porous structures fabricated by electron beam melting, Acta Materialia, 126 (2017) 58–66.

[37]. Ahmadi SM, Campoli G, Amin Yavari S, Sajadi B, Wauthle R, Schrooten J, Weinans H, Zadpoor AA, Mechanical behavior of regular open-cell porous biomaterials made of diamond lattice unit cells, J Mech Behav Biomed Mater, 34 (2014) 106–115. [PubMed: 24566381]

[38]. Rho JY, Kuhn-Spearing L, Zioupos P, Mechanical properties and the hierarchical structure of bone, Med Eng Phys, 20 (1998) 92–102. [PubMed: 9679227]

[39]. Leuders S, Thöne M, Riemer A, Niendorf T, Tröster T, Richard HA, Maier HJ, On the mechanical behaviour of titanium alloy TiAl6V4 manufactured by selective laser melting: Fatigue resistance and crack growth performance, International Journal of Fatigue, 48 (2013) 300–307.

[40]. Rafi HK, Karthik NV, Gong H, Starr TL, Stucker BE, Microstructures and Mechanical Properties of Ti6Al4V Parts Fabricated by Selective Laser Melting and Electron Beam Melting, Journal of Materials Engineering and Performance, 22 (2013) 3872–3883.

[41]. Kasperovich G, Hausmann J, Improvement of fatigue resistance and ductility of TiAl6V4 processed by selective laser melting, Journal of Materials Processing Technology, 220 (2015) 202–214.

[42]. Donachie MJ, Titanium: A Technical Guide, 2nd Edition, ASM International 2000.

[43]. Cheng A, Cohen DJ, Kahn A, Clohessy RM, Sahingur K, Newton JB, Hyzy SL, Boyan BD, Schwartz Z, Laser Sintered Porous Ti-6Al-4V Implants Stimulate Vertical Bone Growth, Ann Biomed Eng, 45 (2017) 2025–2035. [PubMed: 28409291]

[44]. Parthasarathy J, Starly B, Raman S, Christensen A, Mechanical evaluation of porous titanium (Ti6Al4V) structures with electron beam melting (EBM), J Mech Behav Biomed Mater, 3 (2010) 249–259. [PubMed: 20142109]

[45]. Trisi P, Lazzara R, Rao W, Rebaudi A, Bone-implant contact and bone quality: evaluation of expected and actual bone contact on machined and osseotite implant surfaces, Int J Periodontics Restorative Dent, 22 (2002) 535–545. [PubMed: 12516825]

[46]. Hanzlik JA, Day JS, Acknowledged Contributors G: Ingrowth Retrieval Study, Bone ingrowth in well-fixed retrieved porous tantalum implants, J Arthroplasty, 28 (2013) 922–927. [PubMed: 23518432]

[47]. Hanzlik JA, Day JS, Rimnac CM, Kurtz SM, Is There A Difference in Bone Ingrowth in Modular Versus Monoblock Porous Tantalum Tibial Trays?, The Journal of Arthroplasty, 30 (2015) 1073–1078. [PubMed: 25743106]

[48]. Zhao S, Li SJ, Wang SG, Hou WT, Li Y, Zhang LC, Hao YL, Yang R, Misra RDK, Murr LE, Compressive and fatigue behavior of functionally graded Ti-6Al-4V meshes fabricated by electron beam melting, Acta Materialia, 150 (2018) 1–15.

[49]. Onal E, Frith J, Jurg M, Wu X, Molotnikov A, Mechanical Properties and In Vitro Behavior of Additively Manufactured and Functionally Graded Ti6Al4V Porous Scaffolds, Metals, 8 (2018).

[50]. Carpenter RD, Klosterhoff BS, Torstrick FB, Foley KT, Burkus JK, Lee CSD, Gall K, Guldberg RE, Safranski DL, Effect of porous orthopaedic implant material and structure on load sharing with simulated bone ingrowth: A finite element analysis comparing titanium and PEEK, J Mech Behav Biomed Mater, 80 (2018) 68–76. [PubMed: 29414477]

[51]. Levine B, A New Era in Porous Metals: Applications in Orthopaedics, Advanced Engineering Materials, 10 (2008) 788–792.

[52]. Amin Yavari S, van der Stok J, Chai YC, Wauthle R, Tahmasebi Birgani Z, Habibovic P, Mulier M, Schrooten J, Weinans H, Zadpoor AA, Bone regeneration performance of surface-treated porous titanium, Biomaterials, 35 (2014) 6172–6181. [PubMed: 24811260]

[53]. Van der Stok J, Van der Jagt OP, Amin Yavari S, De Haas MF, Waarsing JH, Jahr H, Van Lieshout EM, Patka P, Verhaar JA, Zadpoor AA, Weinans H, Selective laser melting-produced porous titanium scaffolds regenerate bone in critical size cortical bone defects, J Orthop Res, 31 (2013) 792–799. [PubMed: 23255164]

[54]. Ran Q, Yang W, Hu Y, Shen X, Yu Y, Xiang Y, Cai K, Osteogenesis of 3D printed porous Ti6Al4V implants with different pore sizes, Journal of the Mechanical Behavior of Biomedical Materials, DOI 10.1016/j.jmbbm.2018.04.010(2018).

[55]. Greitemeier D, Dalle Donne C, Syassen F, Eufinger J, Melz T, Effect of surface roughness on fatigue performance of additive manufactured Ti–6Al–4V, Materials Science and Technology, 32 (2016) 629–634.

[56]. Rekedal K, Liu D, Fatigue Life of Selective Laser Melted and Hot Isostatically Pressed Ti-6Al-4v Absent of Surface Machining, AIAA 2015.

[57]. Edwards P, Ramulu M, Fatigue performance evaluation of selective laser melted Ti–6Al–4V, Materials Science and Engineering: A, 598 (2014) 327–337.

[58]. Van Hooreweder B, Boonen R, Moens D, Kruth J-P, Sas P, On the Determination of Fatigue Properties of Ti6Al4V Produced by Selective Laser Melting, 53rd AIAA/ASME/ASCE/AHS/ASC Structures, Structural Dynamics and Materials Conference
20th AIAA/ASME/AHS Adaptive Structures Conference
14th AIAA, 2012.

[59]. Wycisk E, Emmelmann C, Siddique S, Walther F, High Cycle Fatigue (HCF) Performance of Ti-6Al-4V Alloy Processed by Selective Laser Melting, Advanced Materials Research, 816–817 (2013) 134–139.

[60]. Kahlin M, Ansell H, Moverare JJ, Fatigue behaviour of notched additive manufactured Ti6Al4V with as-built surfaces, International Journal of Fatigue, 101 (2017) 51–60.

[61]. Greitemeier D, Palm F, Syassen F, Melz T, Fatigue performance of additive manufactured TiAl6V4 using electron and laser beam melting, International Journal of Fatigue, 94 (2017) 211–217.

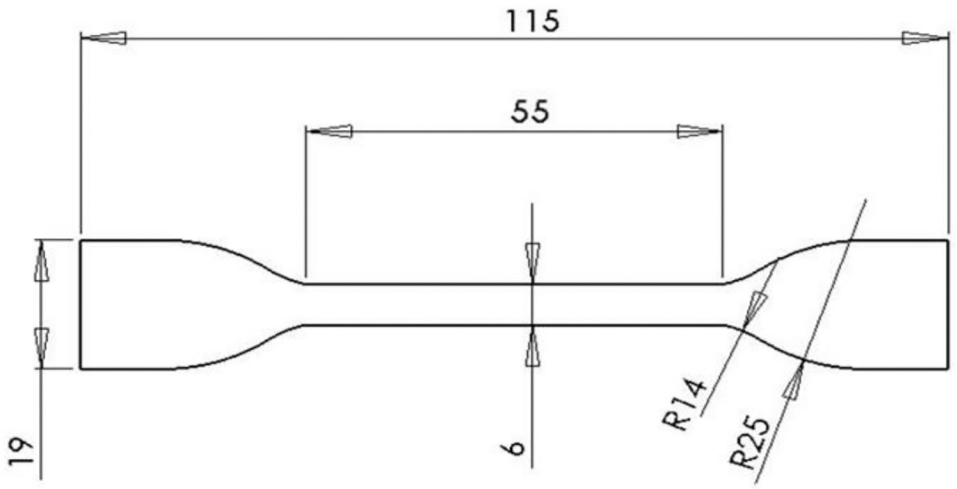

Figure 1.
Schematic of dogbone specimen used for tensile testing, all dimensions in millimeters. Samples were approximately 3.2 mm thick.

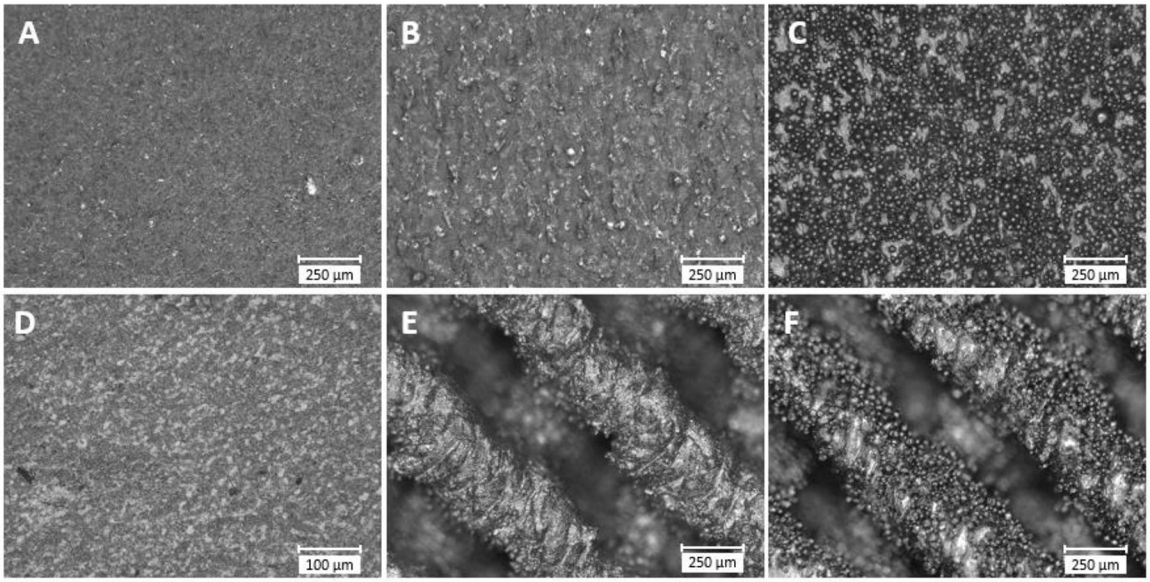

Figure 2.

Optical microscope images showing representative surface topography of sample surfaces, (A) solid rotopolish, (B) solid SILC clean, (C) solid no-surface-treatment, (D) wrought, (E) surface porous SILC clean, (F) surface porous no-surface-treatment.

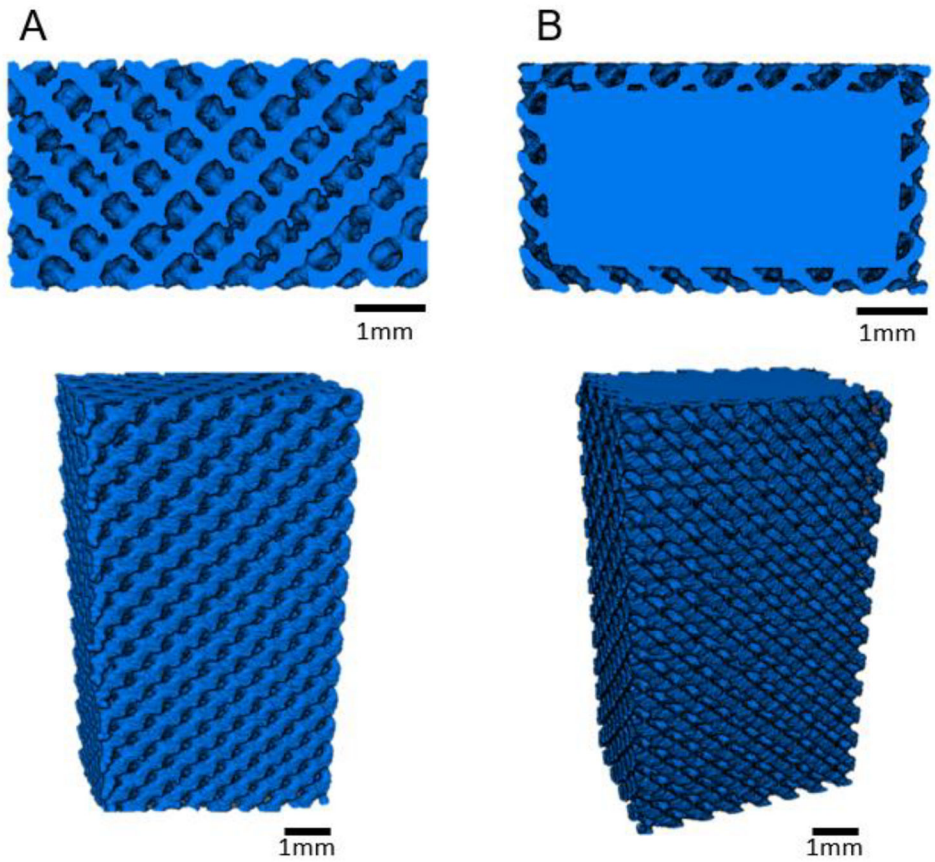

Figure 3.
Representative cross-sectional images of MicroCT reconstructed volume renderings of gauge section of (A) porous and (B) surface porous samples.

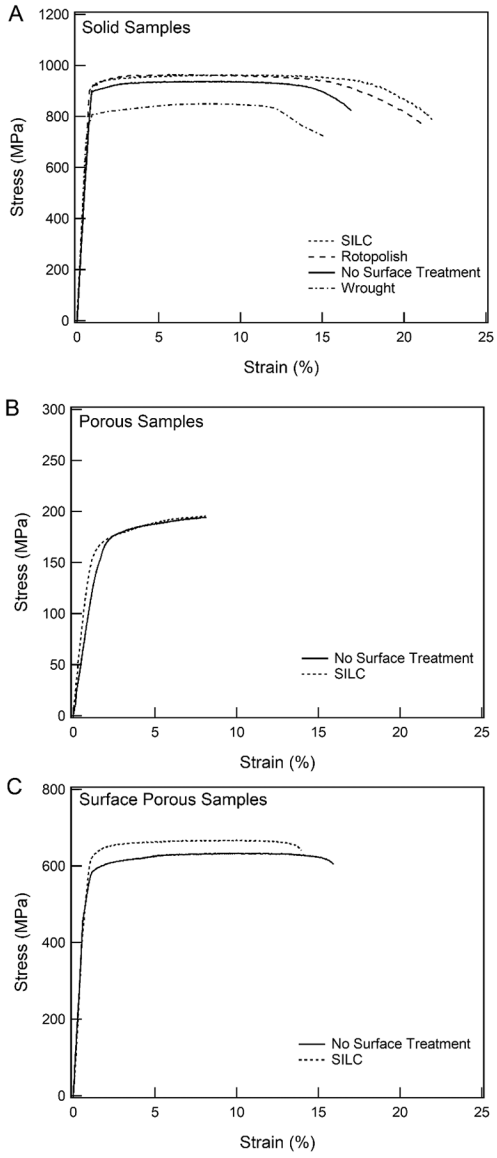

Figure 4.

Representative monotonic tensile stress-strain curves varying surface treatment of (A) solid samples, (B) porous samples, and (C) surface porous samples. Stress calculations based on total area of sample cross-section.

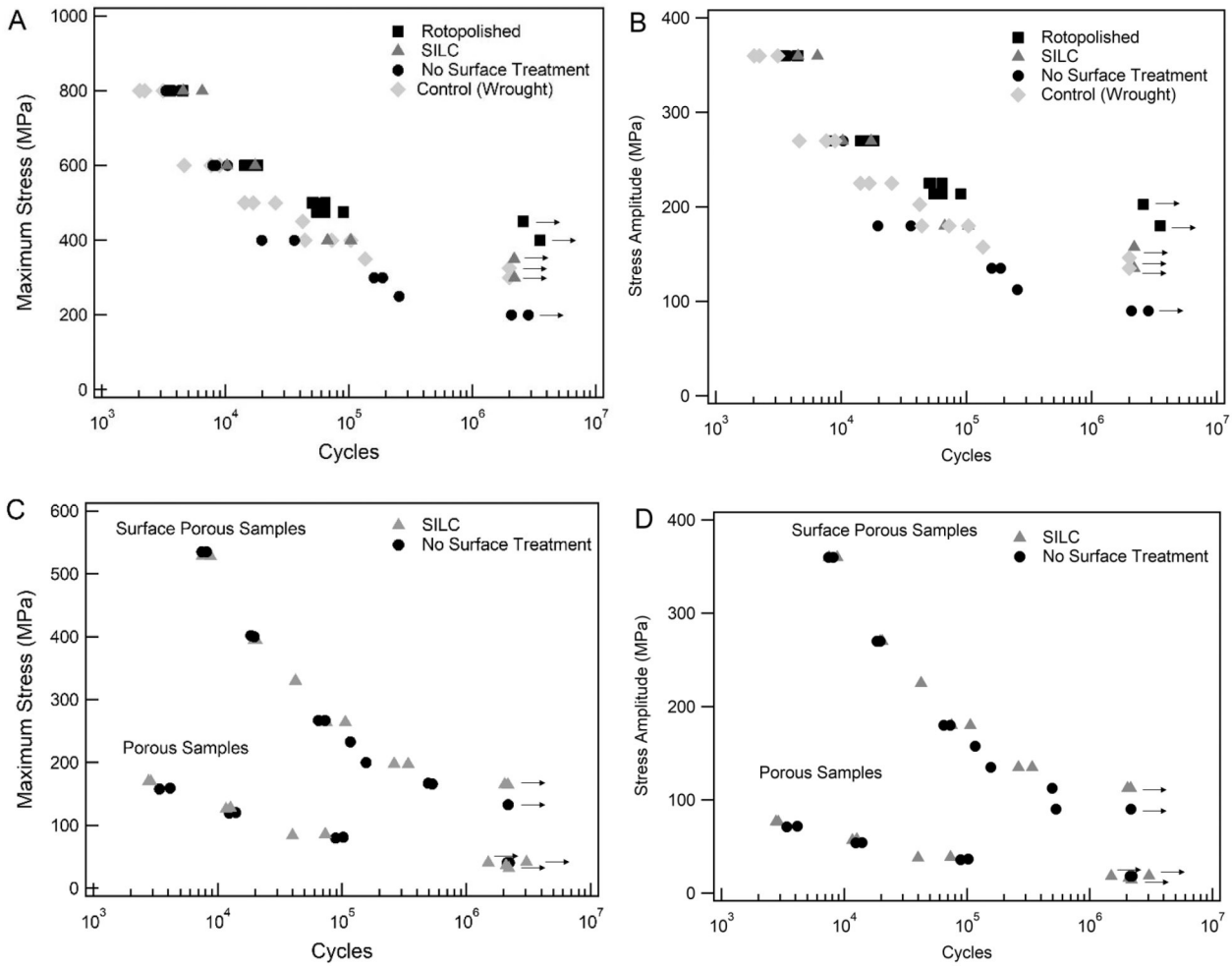

Figure 5.

S-N curve of fatigue behavior of samples with varied surface treatments. (A) Maximum stress applied solid samples and, (B) stress amplitude solid samples, (C) maximum stress porous and surface porous samples, (D) stress amplitude porous and surface porous samples. Arrow denotes runout at greater than 2M cycles.

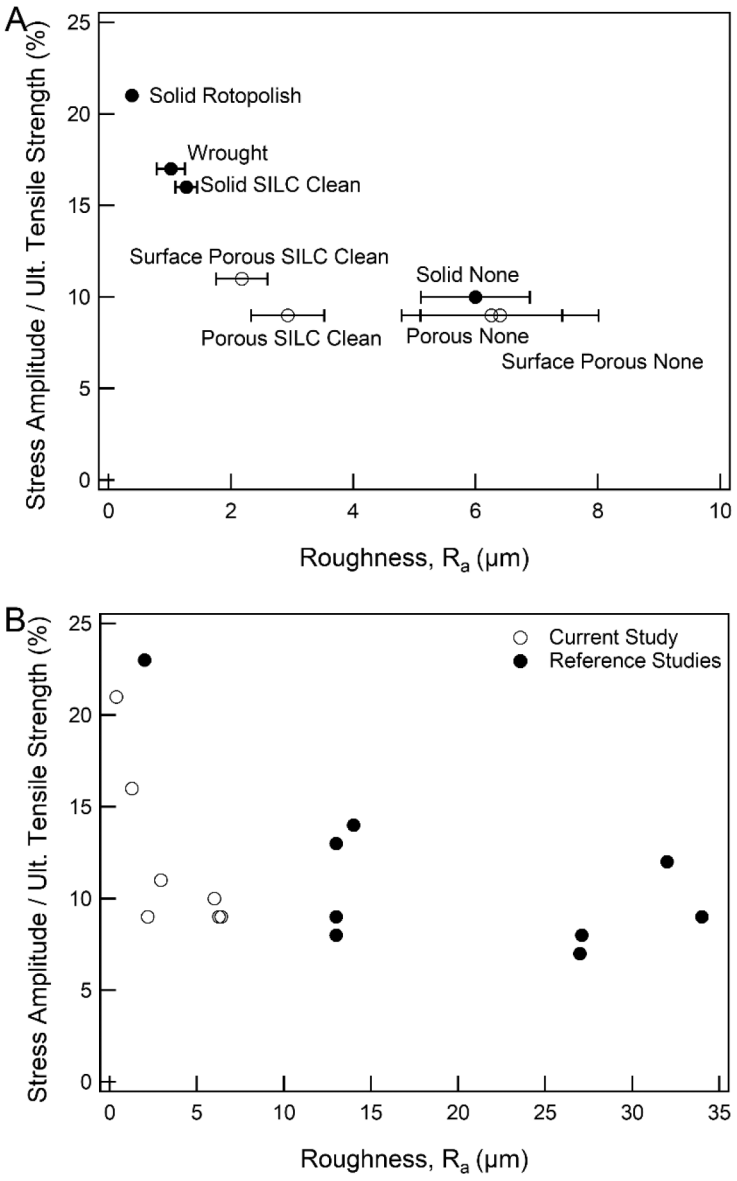

Figure 6.

Fatigue strength normalized by ultimate tensile strength as compared to surface roughness for (A) current study and (B) current study as compared to 3D printed samples from reference studies shown in Table 6.

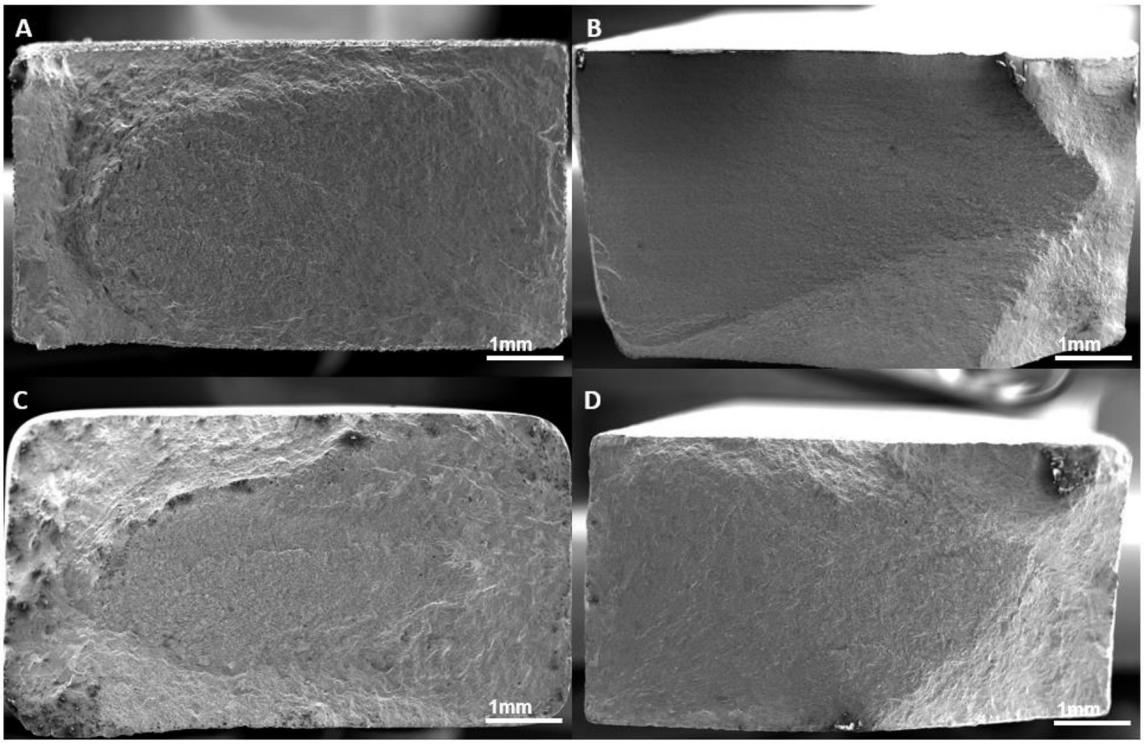

Figure 7.
Fracture surfaces of solid high cycle fatigue samples, (A) no treatment, (B) wrought (C) rotopolished, (D) SILC cleaned.

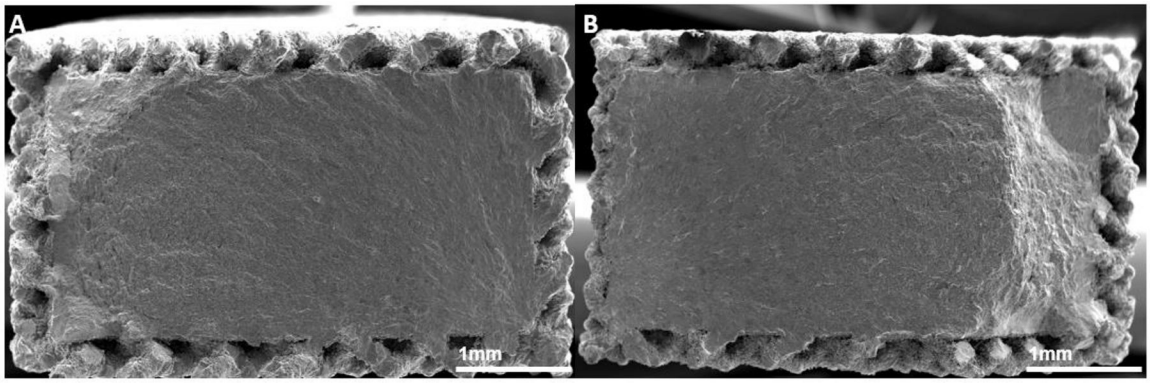

Figure 8.
Fracture surfaces of surface porous high cycle fatigue samples, (A) no treatment, (B) SILC cleaned.

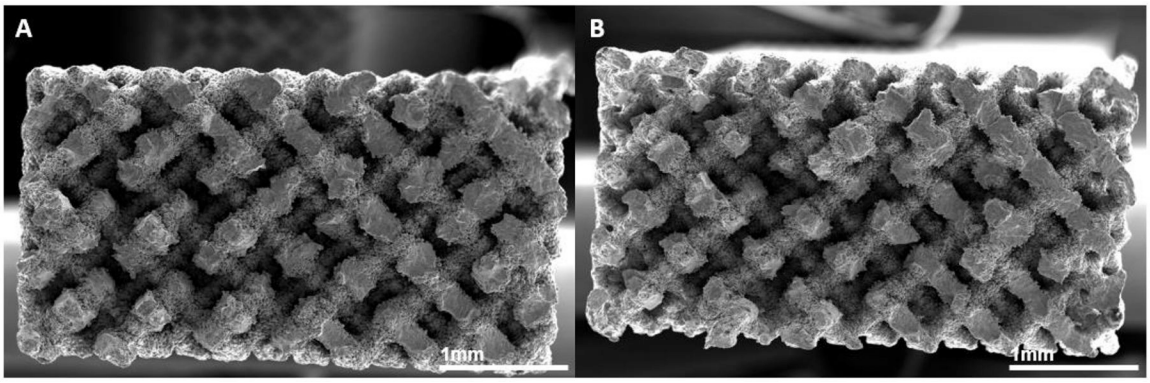

Figure 9.
Fracture surfaces of fully porous high cycle fatigue samples, (A) no treatment, (B) SILC cleaned.

Table 1.

Tensile specimen group roughness values.

Design	Surface Treatment	Roughness, R_a (μm)
Wrought	None	1.02 ± 0.23
Solid	None	6.00 ± 0.89
Solid	Rotopolish	0.38 ± 0.01
Solid	SILC Clean	1.27 ± 0.18
Porous	None	6.40 ± 1.61
Porous	SILC Clean	2.18 ± 0.42
Surface Porous	None	6.26 ± 1.16
Surface Porous	SILC Clean	2.93 ± 0.60

Table 2.

Pore morphology analyses for porous and surface porous specimens.

Design	Surface T reatment	Porosity (%)	Strut Thickness (μm)	Strut Spacing (μm)
		Average ± STD	Average ± STD	Average ± STD
Porous	None	45.5 ± 0.01	175 ± 16	305 ± 11
Porous	SILC Clean	45.8 ±0.01	188 ± 6	319 ± 5
Surface Porous	None	45.4 ± 0.01	174 ± 5	294 ± 6
Surface Porous	SILC Clean	47.3 ± 0.03	195 ± 2	334 ± 28

Table 3.

Monotonic tensile properties of SLM Ti-6Al-4V ELI samples of varying design and surface treatment.

Design	Surface T reatment	Modulus (GPa)	Yield Strength (MPa)	Ultimate TensileStrength (MPa)	Failure Strain (%)
		Average ± STD	Average ± STD	Average ± STD	Average ± STD
Wrought	None	119.3 ± 2.6	806.7 ± 3.2	851.4 ± 5.3	13.5 ± 1.9
Solid	None	108.3 ± 5.4	897.0 ± 2.0	937.5 ± 1.3	16.8 ± 1.9
Solid	Rotopolish	116.3 ± 7.8	883.6 ± 16.9	946.3 ± 16	21.0 ± 0.9
Solid	SILC Clean	108.9 ± 3.1	895.6 ± 1.1	963.0 ± 3.4	20.6 ± 0.8
Porous	None	10.4 ± 0.2	146.6 ± 2.8	194.9 ± 1.9	7.8 ± 0.6
Porous	SILC Clean	14.1 ± 1.9	152.0 ± 2.6	195.5 ± 1.8	9.1 ± 1.1
Surface Porous	None	73.4 ± 0.8	600.7 ± 2.8	661.1 ± 3.3	15.1 ± 1.3
Surface Porous	SILC Clean	70.8 ± 2.1	632.6 ± 7.2	693.9 ± 4.1	14.7 ± 1.5

Table 4.

Fatigue behavior at runout (2M cycles) of Ti-6Al-4V ELI samples of varying design and surface treatments.

Design / Structure	Surface T reatment	Maximum Stress Applied (MPa)	Stress Amplitude (MPa)
Wrought	None	325	146.25
Solid	None	200	90
Solid	Rotopolish	450	202.5
Solid	SILC Clean	350	157.5
Porous	None	40	18
Porous	SILC Clean	40	18
Surface Porous	None	133	59.85
Surface Porous	SILC Clean	165	74.25

Table 5.

Reported porosity and pore morphology from commercial implants and in literature. Values in parentheses are those indicative of reported CAD defined geometry, all others are as fabricated geometry reported in results. All values given as reported in reference.

Ref.	Implant / Sample	Porosity (%)	Average Strut Spacing (μm)	Average Strut Thickness (μm)
[50]	Renovis, Tesera (Titanium)	64.37	607	277
[51]	Stryker, Tritanium (Ti-6Al-4V)	60	616	-
	Biomet, Regenerex (Ti-6Al-4V)	67	300	-
	Zimmer, Trabecular Metal (Tantalum)	75 – 85	550	-
	Smith and Nephew, Stiktite (Titanium)	60	200	-
[28]	Fully porous Human femoral trabecular scaffold (Ti-6Al-4V)	15	177	628
		38	383	454
		70	653	305
[43]	Fully porous Human femoral trabecular scaffold (Ti-6Al-4V)	67	563	-
[52]	Fully porous dodecahedron unit cell scaffold (Ti-6Al-4V)	85 (88)	577 (500)	165 (120)
		89 (88)	596 (500)	160 (120)
		86 (88)	578 (500)	175 (120)
[53]	Fully porous dodecahedron unit cell scaffold (Ti-6Al-4V)	68	(490)	(230)
		88	(490)	(120)
[54]	Cylindrical interconnected channels (Ti-6Al-4V)	-	401 (500)	(300)
		-	607 (700)	(300)
		-	801 (900)	(300)
Current	Fully porous diamond unit cell scaffold (Ti-6Al-4V)	45.5	305	175
	Surface porous diamond unit cell scaffold (Ti-6Al-4V)	45.4	294	174

Table 6.

Mechanical properties and surface roughness of additively manufactured Ti-6Al-4V. All values given as reported in reference.

Ref.	Processing	Maximum Stress Applied (MPa)	Stress Amplitude (MPa)	R	Frequency (Hz)	Ult. Tensile Strength (MPa)	Stress Amplitude/ Ult. Tensile Strength	Roughness, R_a (μm)
[55]	EBM	150	67.5	0.1	150	965	7%	27
	SLM	200	90	0.1	150	1096	8%	13
[40]	EBM	340	153	0.1	50	928	16%	-
	SLM	550	247.5	0.1	50	1219	20%	-
[56]	SLM	230	103.5	0.1	60	936	11%	-
[57]	SLM	200	120	−0.2	20	1035	12%	32
[58]	SLM	126	126	0	75	1170	11%	-
[59]	SLM	467	210	0.1	50	1014	21%	13
[41]	SLM	350	350	−1	82	973	36%	-
[60]	EBM	200	90	0.1	20	1005	9%	34
	SLM	500	225	0.1	20	970	23%	2
	SLM	300	135	0.1	20	968	14%	14
[61]	EBM	140	63	0.1	-	833	8%	27.1
	SLM	185	83.25	0.1	-	949	9%	13
Current	SLM	200	90	0.1	5	937	10%	6.00
		450	202.5	0.1	5	946	21%	0.38
		350	157.5	0.1	5	963	16%	1.27
		40	18	0.1	5	194	9%	6.40
		40	18	0.1	5	195	9%	2.18
		133	59.85	0.1	5	661	9%	6.26
		165	74.25	0.1	5	694	11%	2.93